Consistent Particle Method simulation of solitary wave impinging on and overtopping a seawall

Min Luo[a], Dominic E. Reeve[a], Songdong Shao[b,c], Harshinie Karunarathna[a], Pengzhi Lin[d,*] and Huayang Cai[e]

[a] Zienkiewicz Centre for Computational Engineering, College of Engineering, Swansea University, Swansea SA1 8EN, United Kingdom

[b] Department of Civil and Structural Engineering, University of Sheffield, Sheffield S1 3JD, United Kingdom

[c] College of Shipbuilding Engineering, Harbin Engineering University, Harbin 150001, China

[d] State Key Laboratory of Hydraulics and Mountain River Engineering, Sichuan University, Chengdu 610065, China

[e] Institute of Estuarine and Coastal Research, School of Marine Engineering and Technology, Sun Yat-sen University, Guangzhou 510275, China

Abstract

Tsunamis are among the most destructive natural hazards and can cause massive damage to the coastal communities. This paper presents a first numerical study on the tsunami-like solitary wave impinging and overtopping based on the mesh-free Consistent Particle Method (CPM). The distinct feature of CPM is that it computes the spatial derivatives in a way consistent with the Taylor series expansion and hence achieves good numerical consistency and accuracy. This largely alleviates the spurious pressure fluctuation that is a key issue for the particle method. Validated by the benchmark example of solitary wave impact on a seawall, the CPM model is shown to be able to capture the highly deformed breaking wave and the impact pressure associated with wave impinging and overtopping. Using the numerical model, a parametric study of the effect of seawall cross-sectional geometry on the characteristics of wave overtopping is conducted. It is found that a higher water level can lead to much more intensive overtopping volume and kinetic energy of the overtopping flow, which implies that the coastal areas are at higher risk as the sea level rises. For the purpose of engineering interest, a simple and practical way to estimate the intensity of a real tsunami is presented in terms of the volume and energy of the bulge part of the incident wave.

Keywords: Consistent Particle Method; solitary wave; wave impinging; overtopping

1. Introduction

Tsunamis possess tremendous destructive power and are among the most horrible natural hazards in coastal regions. Upon impact, tsunamis can cause serious damage to coastal structures. After transgressing sea defense structures, the tsunami waves may destroy buildings/facilities and cause inland flooding, often accompanied by heavy casualties. For example, the catastrophic tsunami disasters which occurred in Indonesia in 2006 [1] and in Japan in 2011 [2] caused memorable losses to those societies. For the most recent tsunami disaster triggered by a 7.5-magnitude earthquake in

---

* Corresponding author. Tel.: +86 2885406172; fax: +86 2885405148.
  E-mail: cvelinpz@126.com (P. Lin).

Indonesia, the disastrous wave of height up to 6 meters slammed into the Sulawesi Island at a speed of 800 km per hour [3]. The death toll has until now gone beyond 2000 with almost 3000 people being seriously wounded and more than 70,000 homes were destroyed or damaged. Improved understanding and prediction of tsunami waves and the associated overtopping flows are urgently needed for the mitigation of tsunami hazards.

Solitary waves have resemblances to tsunami waves and hence are frequently used as the substitute in tsunami studies [4, 5], although some studies looked into the differences between a solitary wave and a tsunami wave [6, 7]. The works on both solitary and tsunami waves will be discussed hereafter without emphasizing their differences. Goring [8] derived theoretical formulations based on the Boussinesq equations to generate solitary waves using a piston-type wave maker. After that, this theory has been extensively used in numerical simulations and wave flume/basin experiments. Another strategy of solitary wave generation is to add a source term in either the mass conservation equation [9] or the momentum equation [10, 11] in the internal flow region.

The wave run-up and run-down on a slope beach/seawall have been extensively studied [12, 13]. Some researchers investigated the solitary wave impact pressure/force (of great significance for engineering design) on seawalls [14]. In recent years, the solitary wave interactions with subaqueous structures have been studied such as the bottom-mounted rectangular blocks [15] and circular cylinders [16]. Liang et al. [17] studied the solitary wave interaction with a vertical movable seawall and explored the effects of various factors on the peak impact force experienced by the seawall. Some of the abovementioned studies contain both the numerical simulations and experimental works. The laboratory data enriched the database of solitary wave hydrodynamics and provided benchmarks for the numerical model validations. Although large amount of researches have investigated the solitary wave run-up/run-down and the wave-structure interactions, the studies about the influence of seawall section on the solitary wave overtopping characteristics are limited, which will be the focus of the present study.

With the rapid development of computer technology, the numerical modelling has become increasingly feasible and many numerical algorithms have been developed to simulate different kinds of fluid dynamics problems. The majority of the numerical methods require pre-defined meshes. In recent years, a new category of numerical methods, i.e. particle methods, has achieved significant developments. Two well recognized particle methods are the Smoothed Particle Hydrodynamics (SPH) [18, 19] and Moving Particle Semi-implicit (MPS) method [20]. Without a fixed mesh system, the particle methods are in principle capable of treating the large deformations such as fluid merging and splitting easily and tracking the free surface (or fluid interface) naturally. These provide benefits in simulating the wave hydrodynamics [21-23], wave-structure interaction [24-26], multi-phase flow [27] and flow in porous media [28]. The up-to-date developments of particle method technologies can be referred to Gotoh and Khayyer [29] and Ye et al. [30].

Particle methods have the advantage of being able to capture large deformations, but can suffer from spurious pressure fluctuations [23], which further cause the misestimation of the peak impact pressure [31]. One major cause is that the derivative approximation schemes introduce numerical errors particularly for the irregular particle distributions [32]. Substantial researches have been devoted to reducing the unphysical noises by developing derivative computation schemes of higher-order accuracy and/or with better energy conservation properties [33, 34] and by using numerical schemes such as diffusive terms [35-37] and particle shifting [38, 39]. The Consistent Particle Method (CPM) was developed to enhance the derivative computation from a new perspective [32]. Different from the kernel approximation schemes in SPH and the weighted-average particle interaction models in MPS, the CPM computes the first- and second-order derivatives simultaneously based on the Taylor series expansion [32]. In this way, the numerical consistency that is a key issue in the derivative approximation of particle methods can be achieved and hence the numerical accuracy is improved. This further leads to an accurate prediction of the fluid pressure in violent free surface flow [40] and two-phase flow [41] problems.

This work presents the first application of the CPM model for solitary wave overtopping and impinging on a seawall in coastal applications. In the paper, the key formulations and distinct features of CPM are introduced. The numerical model is validated against the published experimental data and numerical results of Hsiao and Lin [14]. The studies on wave profile, wave elevation, and wave impact pressure/force serve as a comprehensive demonstration of the CPM's capability in predicting the coastal breaking waves. Using the validated model, the volume and kinetic energy of the overtopping waves with different seawall sections are parametrically studied. A simple and practical way of estimating the intensity of tsunami is recommended.

2. CPM methodology

2.1. Governing equations

CPM solves the governing equations of the conservations of mass and momentum, i.e. the Navier-Stokes equations, as follows

$$\frac{1}{\rho}\frac{\mathrm{D}\rho}{\mathrm{Dt}} + \nabla \cdot \mathbf{v} = 0 \tag{1}$$

$$\frac{\mathrm{D}\mathbf{v}}{\mathrm{Dt}} = -\frac{1}{\rho}\nabla \mathrm{p} + \nu\nabla^2\mathbf{v} + \mathbf{g} \tag{2}$$

where ρ is the density of a fluid, $\mathbf{v}$ the particle velocity vector, p the fluid pressure, t the time, ν the kinematic viscosity of a fluid and $\mathbf{g}$ the gravity acceleration. The fluid domain is discretized by Lagrangian particles that carry fixed masses and move under the forces governed by Equation (2).

2.2. Two-step semi-implicit solution scheme

There are two main approaches to solve the governing equations. The first approach relates the fluid pressure and density by an equation of state, and hence treats the fluid as weakly-compressible. The standard SPH adopts this strategy. Another approach solves for fluid pressure implicitly by a two-step algorithm and imposes the fluid incompressibility [20, 22, 42] and CPM adopts the latter approach. In the predictor step, the temporary particle velocities ($\mathbf{v}^*$) and positions ($\mathbf{r}^*$) are computed by neglecting the pressure gradient term:

$$\mathbf{v}^* = \mathbf{v}^{(k)} + \left[\nu \nabla^2 \mathbf{v}^{(k)} + \mathbf{g} \right] \Delta t \tag{3}$$

$$\mathbf{r}^* = \mathbf{r}^{(k)} + \mathbf{v}^* \Delta t \tag{4}$$

where $\mathbf{v}^{(k)}$ and $\mathbf{r}^{(k)}$ are the particle velocity and position in the k-th (previous) time step, respectively. $\Delta t = t^{(k+1)} - t^{(k)}$ is the time step size, governed by the Courant-Friedrichs-Lewy (CFL) condition:

$$\frac{v_{max} \Delta t}{l_0} \leq C_{max} \tag{5}$$

where v_{max} is the maximum particle velocity, l_0 the initial particle spacing and the coefficient C_{max} selected to be 0.25.

In the corrector step, a pressure Poisson equation (PPE) is solved as follows

$$\nabla \cdot \left(\frac{1}{\rho^*} \nabla p^{(k+1)} \right) = \frac{1}{\Delta t^2} \frac{\rho^{(k+1)} - \rho^*}{\rho^{(k+1)}} \tag{6}$$

The fluid incompressibility condition is enforced by setting the fluid density at the current time step ($\rho^{(k+1)}$) to the initial value (ρ_0). The intermediate fluid density (ρ^*) of a particle is evaluated by taking the particle summation within its influence domain (the influence radius $r_e = 2.1l_0$) [41].

Applying the derivative computation scheme presented in following Section 2.3 to the left-hand side of Equation (6), a linear equation system with sparse and non-symmetric coefficients can be obtained. With the solved pressures, the velocities and positions of fluid particles can be updated as

$$\mathbf{v}^{(k+1)} = \mathbf{v}^* - \left(\frac{\nabla p}{\rho} \right)^{(k+1)} \Delta t \tag{7}$$

and

$$\mathbf{r}^{(k+1)} = \mathbf{r}^{(k)} + 0.5 \left(\mathbf{v}^{(k)} + \mathbf{v}^{(k+1)} \right) \Delta t \tag{8}$$

4

2.3. Derivative computation based on Taylor series expansion

The Taylor series expansion for a smooth function f(x, y) in the vicinity of a reference particle (x_0, y_0) can be expressed as

$$f(x, y) = f_0 + hf_{,x0} + kf_{,y0} + \frac{1}{2}h^2 f_{,xx0} + hkf_{,xy0} + \frac{1}{2}k^2 f_{,yy0} + O(r^3) \tag{9}$$

where $h = x - x_0$, $k = y - y_0$, $f_0 = f(x_0, y_0)$, $f_{,x0}$ is the first-order derivative of function f with respect to x at (x_0, y_0), and $f_{,xy0}$ the second-order derivative of function f with respect to x and y at (x_0, y_0), and the same definitions also apply to other derivatives. By writing Equation (9) for each of the neighboring particles, the following equation system can be obtained

$$[\mathbf{A}]\{\mathbf{Df}\} - \{\mathbf{f}\} = 0 \tag{10}$$

where $[\mathbf{A}]$ is a function of relative particle positions (i.e. h and k), $\{\mathbf{f}\}$ is a combination of the variable differences between the reference particle and its neighboring particles, (i.e. $f - f_0$), and $\{\mathbf{Df}\}$ is a vector including the five derivatives in Equation (9). Solving Equation (10) using the weighted-least-square approach, the first- and second-order derivatives can be obtained simultaneously as follows [32]

$$\frac{\partial f_i}{\partial x} = \sum_{j \neq i}\left[w_j^2 \left(a_1 h_j + a_2 k_j + 0.5a_3 h_j^2 + a_4 h_j k_j + 0.5a_5 k_j^2 \right)\left(f_j - f_i \right)\right] \tag{11}$$

and

$$\frac{\partial^2 f_i}{\partial x^2} = \sum_{j \neq i}\left[w_j^2 \left(c_1 h_j + c_2 k_j + 0.5c_3 h_j^2 + c_4 h_j k_j + 0.5c_5 k_j^2 \right)\left(f_j - f_i \right)\right] \tag{12}$$

where w_j is the weighting function used in the weighted-least-square scheme. This weighting function is essentially different from the kernel in SPH and the weighting function in the particle interaction model of MPS, both of which serve as the weighting in the weighted average calculation of function value or derivatives. Coefficients a_i (i = 1, 2, …, 5) in Equation (11) and c_i (i = 1, 2, …, 5) in Equation (12) are the coefficients generated by the weighted-least-square scheme (refer to Equation (21) in [32]). Substituting the general variable f in Equations (11) and (12) with particle velocity or pressure leads to the required derivative computations.

2.4. Free surface and solid boundaries

The free surface particles are recognized by the "arc" method [43]. If any arcs of a circle around a reference particle are not covered by the circles of its neighbors, then this reference particle is a free surface particle (the reader is referred to [32] for more details). The essential boundary condition, i.e. p = 0, is enforced on the free surface particles.

Impermeable walls are modelled by the fixed particle approach [20, 22, 42], i.e. one layer of wall particles placed on the physical wall and two more layers of dummy particles outside the wall to

5

ensure that the fluid density is not truncated near the solid boundary. The moving wave paddle is simulated by updating the positions of wall and dummy particles in accordance with the physical wall motion. The pressures on the wall particles are solved in the same way as the fluid particles. The pressures on dummy particles are related to the pressure of the nearest wall particles by the hydrostatic relationship, satisfying the Neumann boundary condition $\partial p/\partial \mathbf{n} = -\rho \mathbf{g} \cdot \mathbf{n}$, where $\mathbf{n}$ is the outward unit vector of the solid boundary.

3. Benchmark study – Solitary wave impact on an impermeable seawall

The solitary wave impact on an impermeable seawall is simulated by CPM in comparison with the experimental data and the finite difference method simulations in Hsiao and Lin [14]. The solitary waves are generated by a piston type wave maker, whose motion is determined by the theory presented in Goring [8].

3.1. Computational parameters

Fig. 1 sketches the physical domain of the problem. In the experimental study of Hsiao and Lin [14], the sloping beach starts at 10 m from the initial position of the wave paddle. To balance the computational efficiency and an adequate flume length to capture the key physics, the numerical simulation in [14] adopts a shorter wave flume in which the slope beach starts at x = 7 m. For a fair comparison, the CPM simulations adopt the same computational domain as [14]. The type 2 and type 3 solitary waves in [14] that induce significant wave overtopping are studied (see Table 1). In CPM simulations, the initial particle spacing of 0.005 m and fixed time step of 0.0005 s are used (satisfying the CFL condition). The latest OpenMP parallel CPM code [44] is used. The computational time per 1000 time steps for type 2 (87,841 particles) and type 3 (104,944 particles) waves is about 0.75 hour and 0.86 hour, respectively, on a laptop with Intel(R) Core i7-7500U (4 threads).
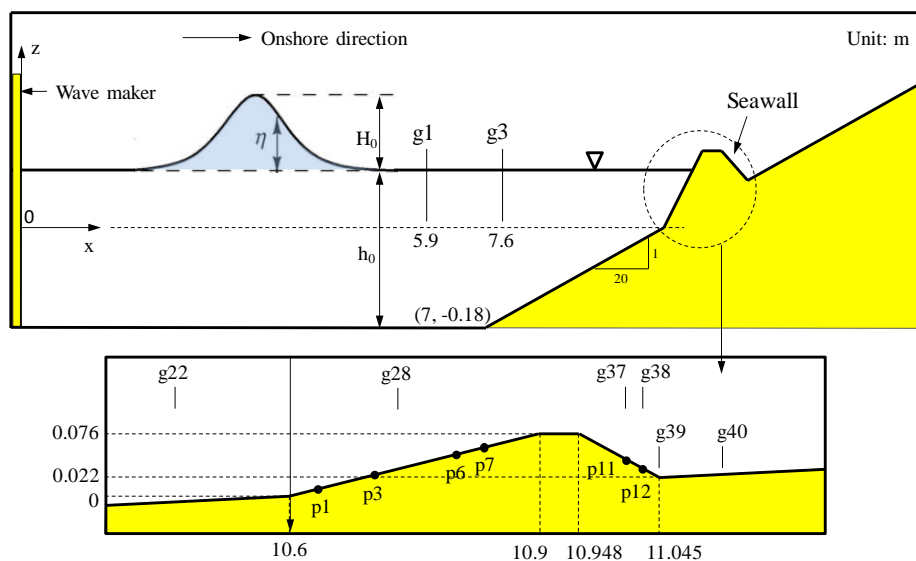

Fig. 1. Dimensions of computational domain and positions of wave gauges and pressure sensors

The wave elevations are studied at eight positions as shown in Fig. 1, whose x coordinates from the initial paddle position are 5.9 m (g1), 7.6 m (g3), 10.462 m (g22), 10.732 m (g28), 11.005 m (g37), 11.024 m (g38), 11.045 m (g39) and 11.12 m (g40), respectively. The wave pressures are studied at six positions on the seawall (see Fig. 1). The x coordinates of these measurement points are 10.63 m (p1), 10.7 m (p3), 13.8 m (p6), 13.83 m (p7), 14.01 m (p11) and 14.02 m (p12), respectively.

Table 1. Parameters of solitary waves in Hsiao and Lin [14]

Case number	h_0 (m)	H_0 (m)	$\varepsilon = H_0 / h_0$
Type 2	0.22	0.0638	0.35
Type 3	0.256	0.0589	0.23

3.2. Type 2 solitary wave

Fig. 2 shows the type 2 solitary wave profiles predicted by CPM in comparison with the results in Hsiao and Lin [14]. Generally, CPM captures the breaking and post-breaking processes of the solitary wave accurately. As the wave propagates onshore, a plunging breaker forms and entraps some air (Fig. 2a and b). The plunging wave slams on the seawall, generating energetic bubbly flows (Fig. 2c). This slamming impact is one of the main factors that causes the damages of parapets or other facilities on the seawall [45]. In CPM results, the bubbly flow is not reproduced as the air phase is not modeled explicitly. Immediately following a plunging wave impact, a jet flow towards the leeside (Fig. 2d) is evident. The jet flow falls under gravity (Fig. 2e) and then impinges on the leeside slope and the field after the seawall (Fig. 2f). Some air is entrapped between the jet flow and the back slope, which can be seen from both the experimental and CPM (air void as air is not modeled) snapshots. The jet flow impingement may cause structural failures of the seawall back slope and erosion of the foundation behind the seawall [46]. The wave elevations at typical positions are presented in the left column of Fig. 3. The CPM solutions are in good agreement with the experimental and numerical results of [14]. This demonstrates the accuracy of CPM to reproduce the highly deformed breaking waves.
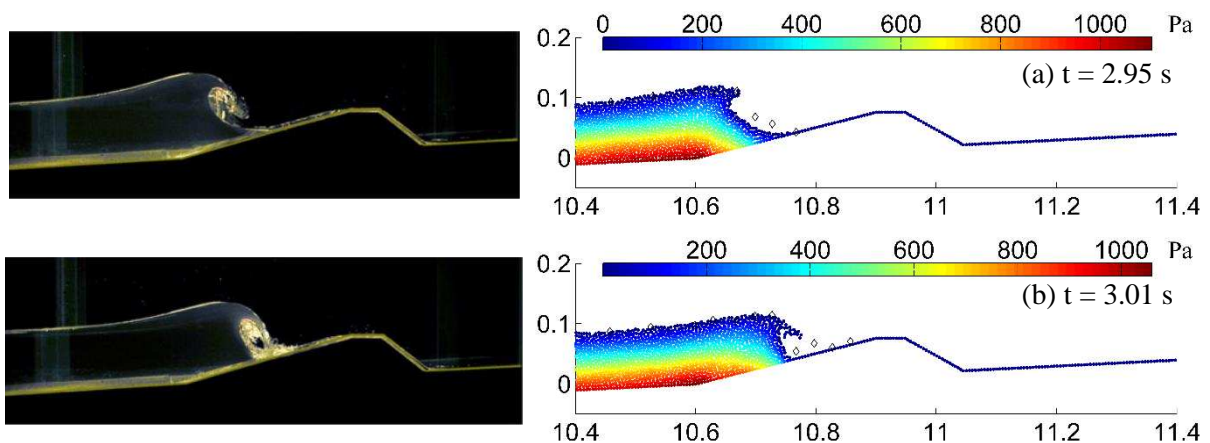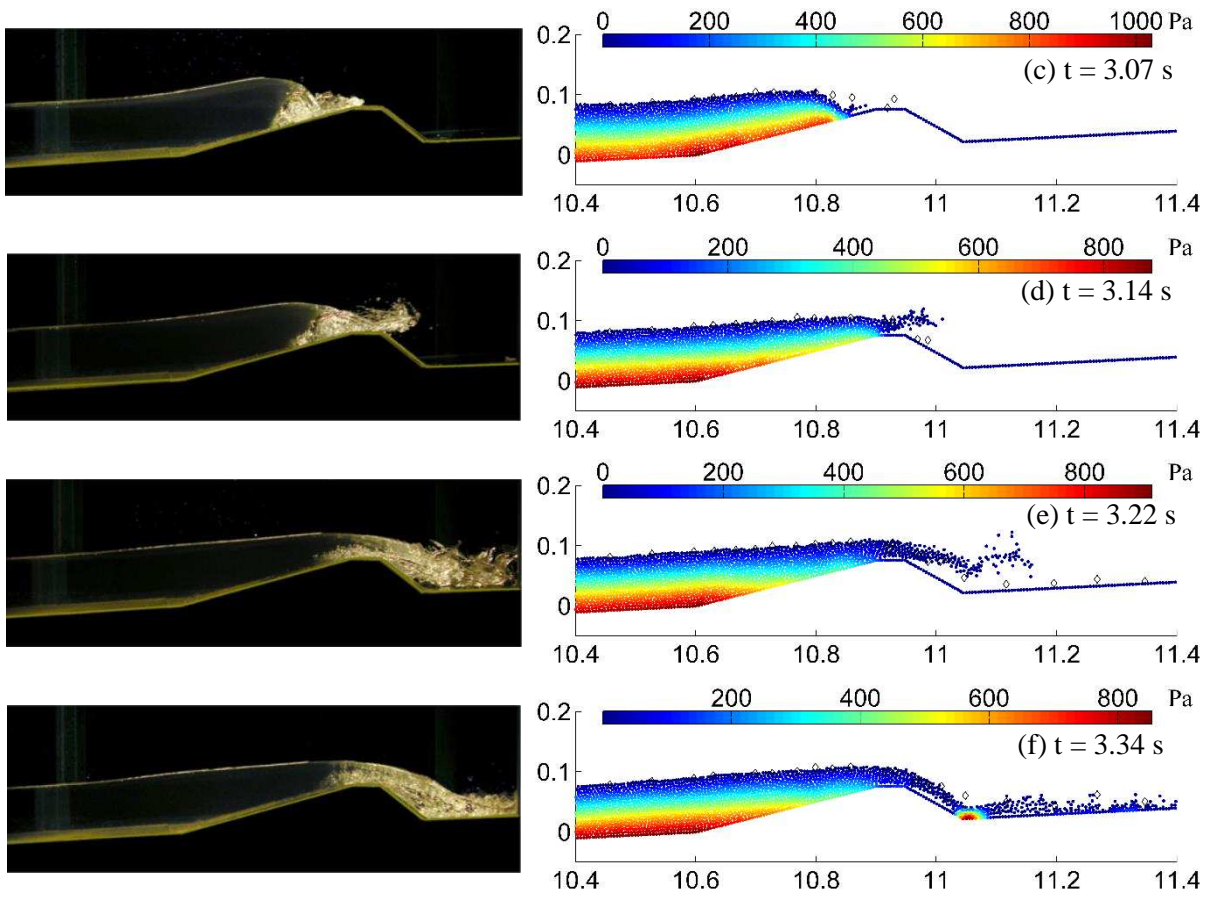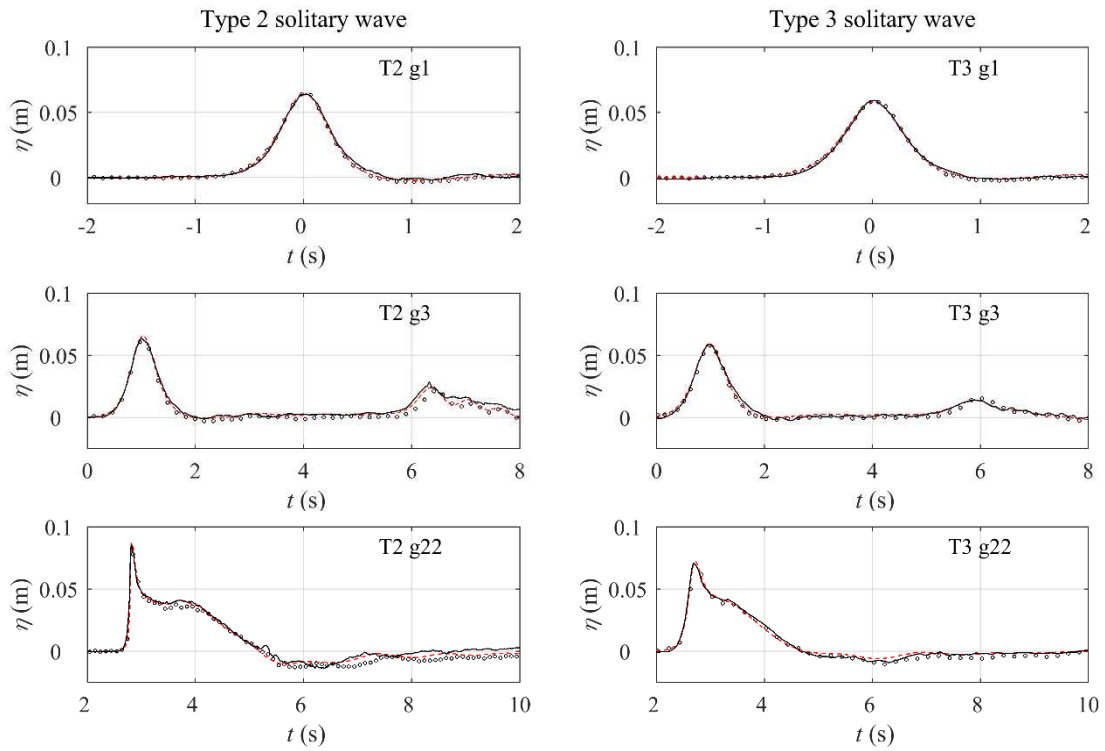
Fig. 2. Type 2 solitary wave profiles: left column - laboratory images in [14]; right column - CPM particle distributions with pressure contour and experimental (diamond) results in [14]
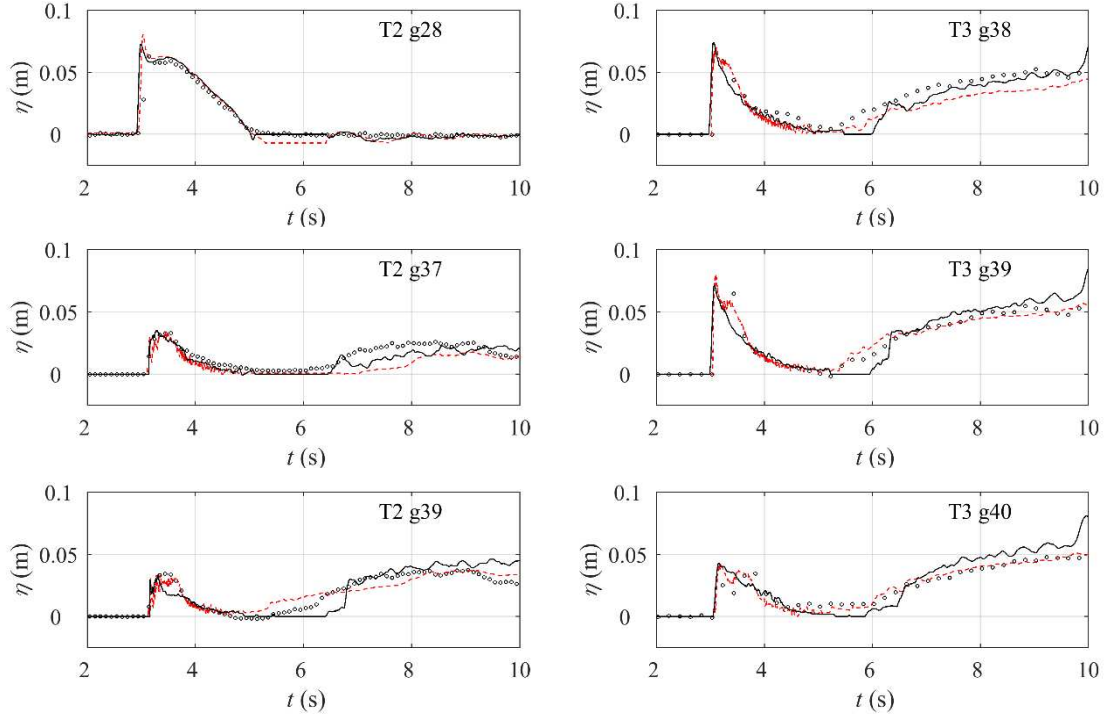
Fig. 3. Wave elevations at typical positions: CPM results (black solid line), numerical (red dash line) and experimental (black circle) results in [14]

The left column of Fig. 4 shows the wave impact pressures on the seawall. The CPM solutions agree well with both the experimental data and the numerical results in Hsiao and Lin [14]. The peak impact pressures are successfully predicted except p12, which is near the bottom of the leeside of the seawall. The overtopping flow impinges on the back slope and entraps air. Because of aeration, the wave evolves into the bubbly flow (see Fig. 2e and f). In a single-phase simulation ignoring the air phase, the air entrapment region that should be occupied by air is empty. When the wave is approaching the structure and has not fully occupied the air entrapment region, some structural particles are recognized as inner fluid particles and hence their pressures should be obtained by solving the PPE. Because of the void (includes air in reality), the influence domains of these wall particles that are adjacent to the void and recognized as inner particles are truncated. This induces numerical errors to the intermediate fluid densities of these structural particles. Specifically, the computed densities tend to be smaller. Although the Laplacian operator of pressure (the left hand side of the PPE) is computed with good accuracy, the errors in fluid density (the right hand side of the PPE) lead to smaller pressures and pressure fluctuations. This is why the wave impact pressure p12 is smaller than the experimental result and shows some fluctuations. To capture the air entrapment in detail and enhance the pressure result would require a two-phase simulation that allows for the compression of air. Another consequence of the numerical noise is that the induced spurious fluctuations tend to dominate the fluid turbulence and hence there is no sense to add a turbulence model in simulation. Ignoring the turbulence model is attributed to another reason of the discrepancies between the numerical and experimental results.

9

Although ignoring the air phase misses some local physics and induces some unphysical pressure fluctuations, the single-phase model is able to predict the general wave impinging and overtopping processes as demonstrated by the results of wave profile, wave elevation and wave impact pressures at the locations other than p12. In addition, the single-phase simulation costs much less (the exact number is dependent on the ratio between water and air particles) time than the water-air two-phase simulation. Taking the balance between the accuracy and efficiency, the current study uses the single-phase simulation.
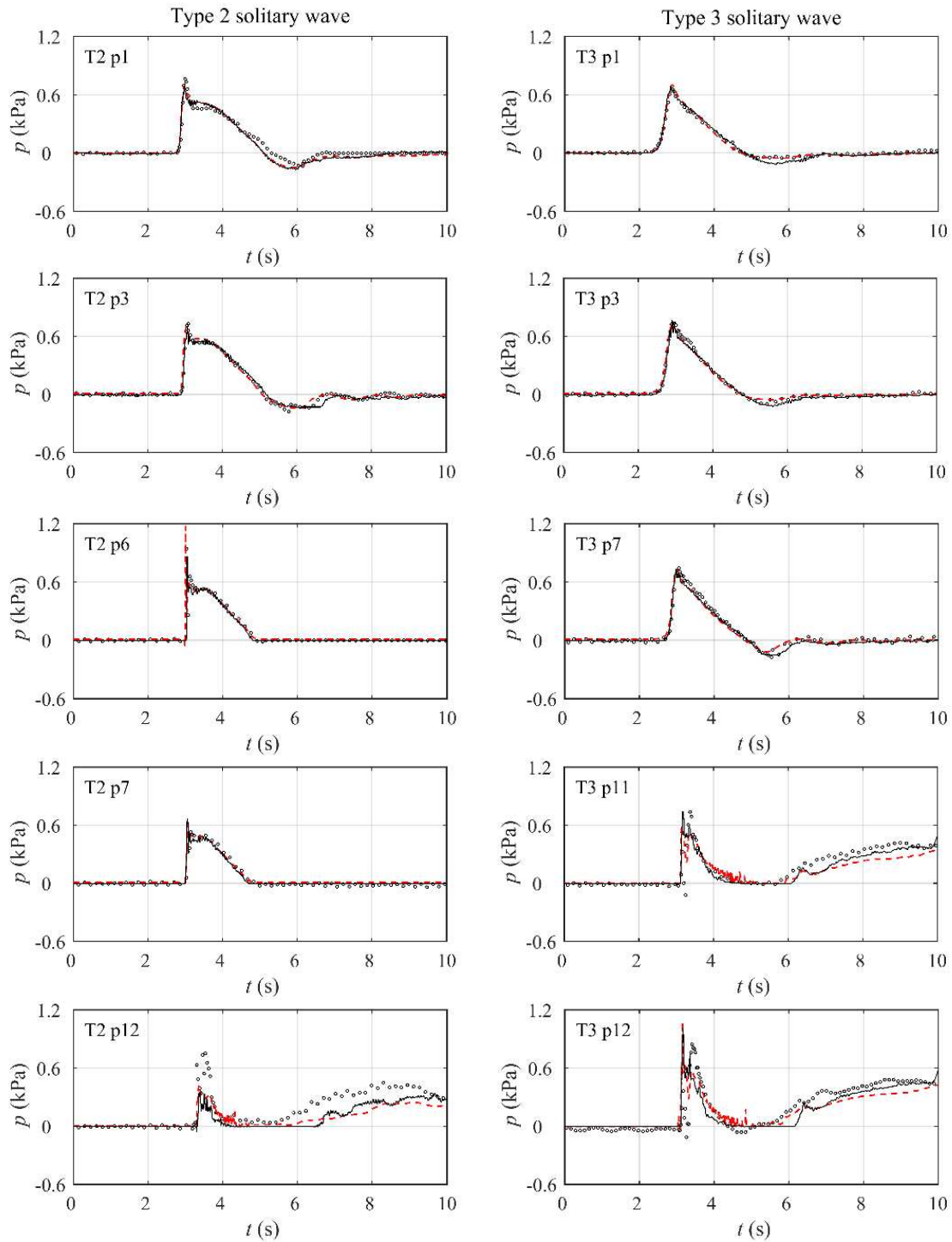

Fig. 4. Dynamic pressures on the seawall induced by solitary wave impinging: CPM results (black solid line), numerical (red dash line) and experimental (black circle) results in [14]

Integrating the wave pressures along the seawall shall give the horizontal (F_H) and vertical (F_V) components of the wave force applied onto the seawall, as presented in Fig. 5. On the seaward side, the CPM solutions are in better agreement with the experimental data than the numerical results in [14]. Since the seaward side slope of the seawall is very gentle, the horizontal force on the seawall is small and hence the seawall has good overturn-resistance capability. On the other hand, this gentle-slope seawall also applies a small resistance force to the wave and thus induces less wave reflections. Therefore, the waves can run-up the seaward slope and over the crest with a larger velocity, and induce larger dynamic forces on the structures and land behind the seawall, causing more damages. On the leeward side, the wave forces predicted by CPM are smaller than the numerical solutions and experimental results in [14]. It is hypothesized that the wave flow transgressing the seawall is very thin and a large amount of overtopping flow particles are recognized as free surface particles (see the red particles above the back slope of the seawall in Fig. 2f) and hence have zero pressure, which leads to smaller wave forces.
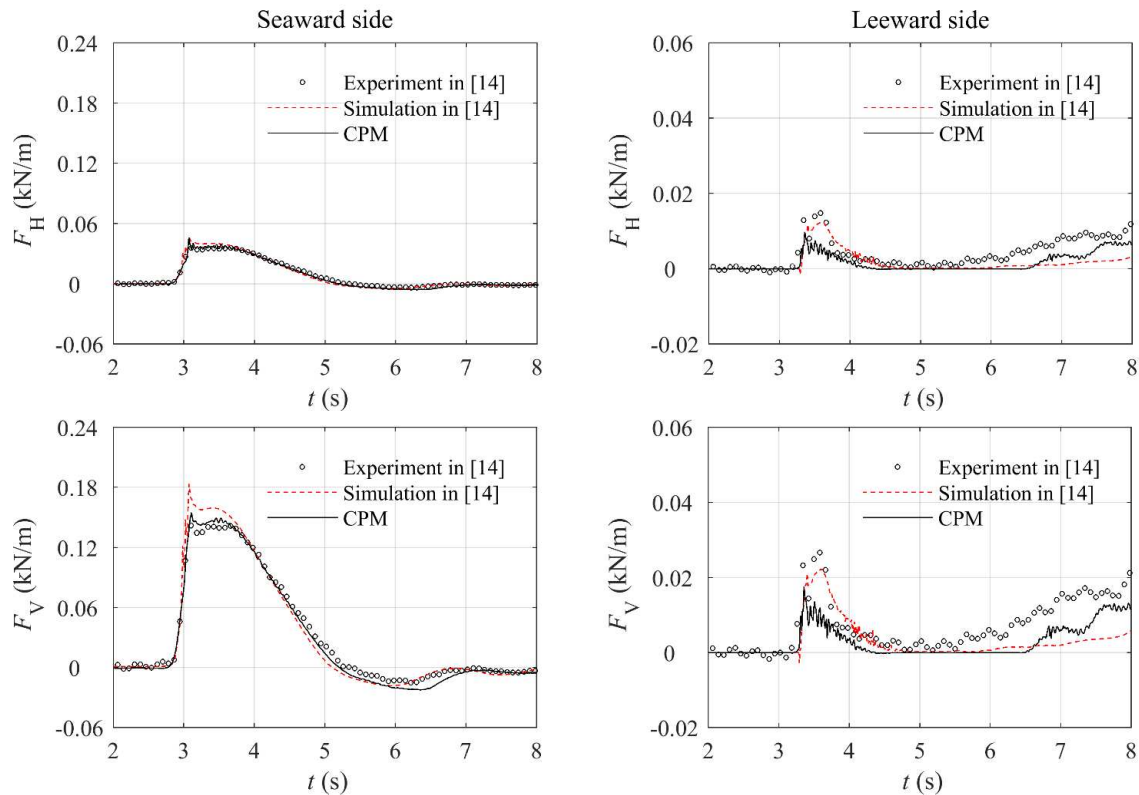

Fig. 5. Horizontal (F_H) and vertical (F_V) components of dynamic wave forces on the seawall induced by type 2 solitary wave

3.3. Type 3 solitary wave

The type 3 solitary wave is also studied. Because the water depth is larger, the type 3 wave does not break on the seaward side of the seawall (Fig. 6a). Instead, it overtops the crown of the seawall straightforwardly and collapses on the back slope of the seawall (Fig. 6b). The overtopping flow induces air entrapment (the "white bubble" in experiment and "void" in CPM simulation in Fig. 6c). Similar to type 2 solitary wave, bubbly flows are generated subsequently because of the aeration (Fig.

11

6d). Since the present CPM model does not consider the air phase, the aeration effect and the bubbly flows cannot be reproduced. Hence, some discrepancies exist between the CPM and experimental snapshots at t = 3.33 s. The water keeps moving to the leeward of the seawall, which can cause serious damages to the buildings and facilities behind the seawall as well as inland flooding. After inundating the inland, the waves come back and swash the foot of the back slope. The turning over flows may cause damages and erosions to the foundation of the seawall. This is one of the three main collapse mechanisms of the seawall damages in the Fukuoka Tsunami in 2011 [45]. As shown in the right column of Fig. 3, the wave elevations on the seaward and leeward sides of the seawall predicted by CPM are in good agreement with the experimental and numerical results in [14]. And so do the CPM solutions of wave impact pressures (the right column of Fig. 4) and the wave impact forces on the front and back slope of the seawall (Fig. 7). This shows the capability of CPM to simulate the highly deformed breaking waves and the accompanied wave impact pressures and force.
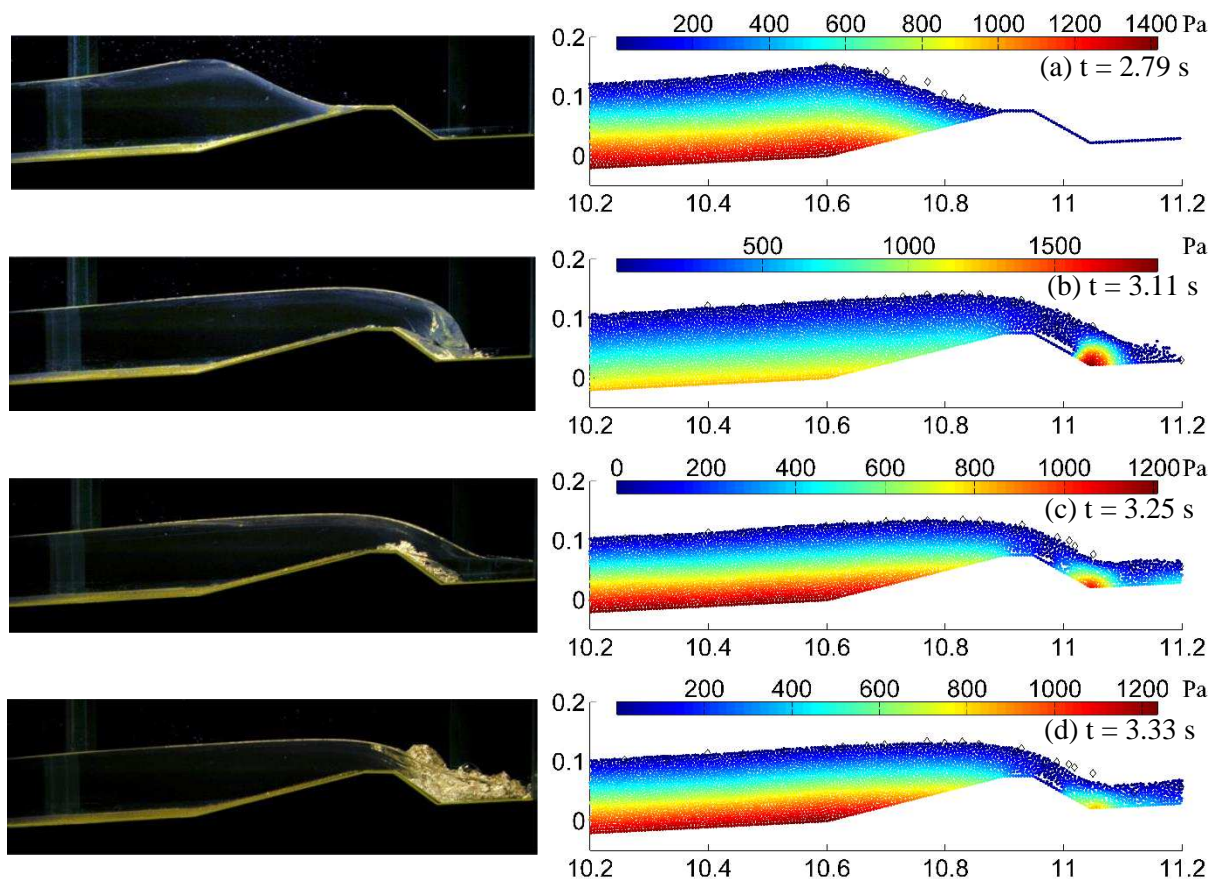

Fig. 6. Type 3 solitary wave profiles: left column - laboratory images in [14]; right column - CPM particle distributions with pressure contour and experimental (diamond) results in [14]

To demonstrate the spatial convergence of the CPM model, type 3 solitary wave is studied by using two additional particle spacing (l_0), i.e. 0.01 m and 0.0075 m. Fig. 8 presents the wave elevation at g22 and wave impact pressure at p7 for different particle sizes. In the coarsest case (l_0 = 0.01 m), both the wave elevation and pressure show phase lags and have slightly smaller amplitudes compared to the experimental results in [14]. In the case of l_0 = 0.0075 m, there are no evident phase lags and

the amplitudes are predicted well. The results of the finest case ($l_0 = 0.005$ m) are very close to those of $l_0 = 0.0075$ m, but they do show less pressure fluctuations and slightly better agreements with the experimental data in general. This shows the particle size convergence of the CPM model. The particle spacing $l_0 = 0.005$ m is adopted in the parametric study of wave overtopping characteristics with seawall section (presented in Section 4).
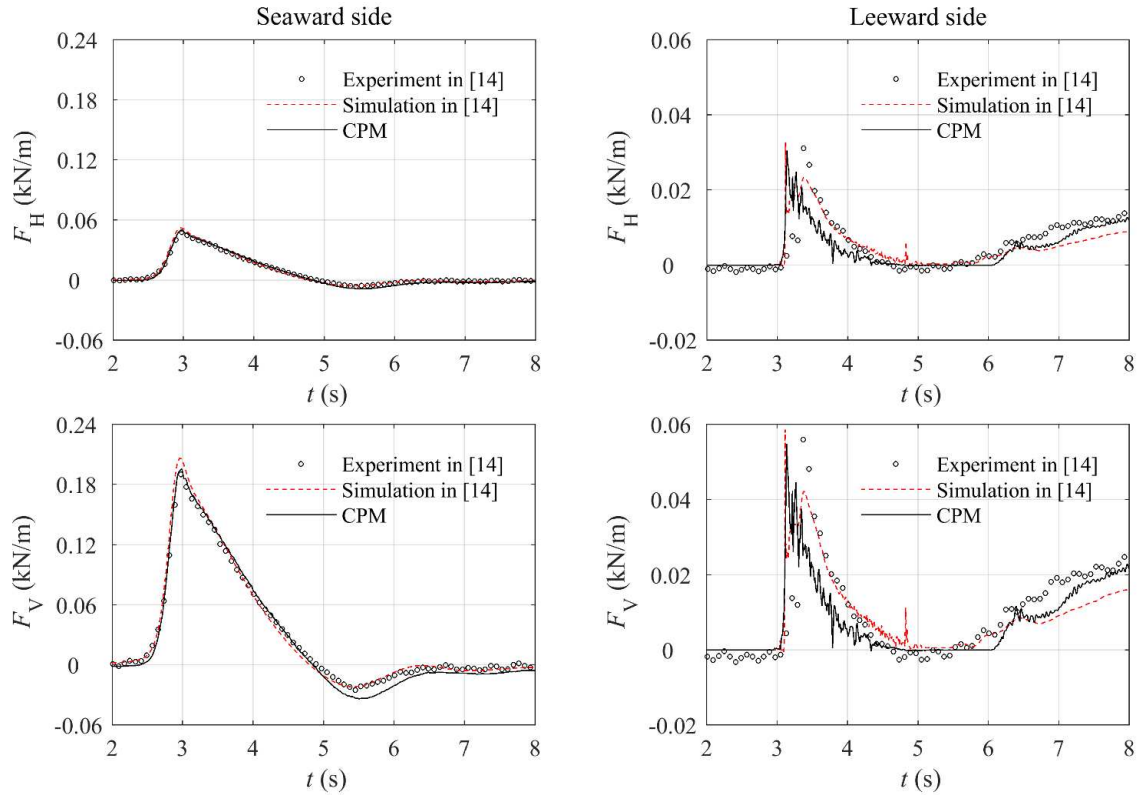

Fig. 7. Horizontal (F_H) and vertical (F_V) components of dynamic wave forces on the seawall induced by type 3 solitary wave
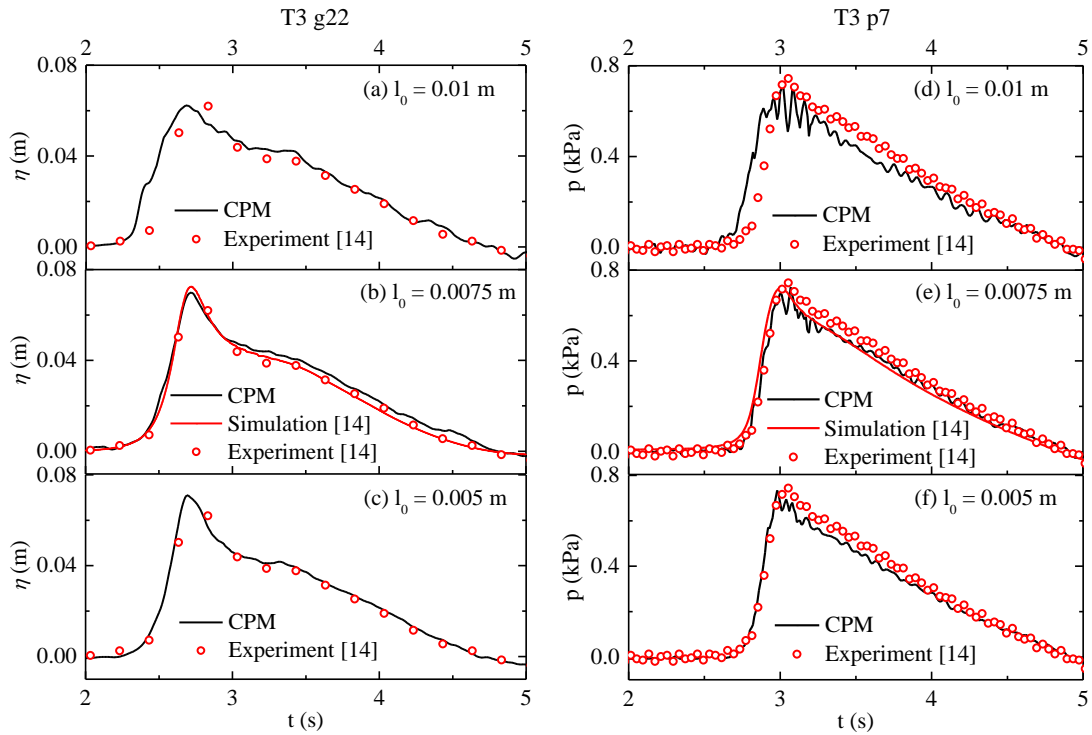
Fig. 8. Comparison of T3 g22 and T3 p7 at initial particle spacing of 0.01m, 0.0075m and 0.005 m, respectively – CPM results vs. experiment and simulation in [14]

4. Influence of seawall section on solitary wave overtopping

Wave overtopping is amongst the most important factors in the design of coastal defense structures. To date, there has been very little published on the relationship between the seawall cross-sectional geometry and solitary wave overtopping. To fill this gap, this section studies the volume and kinetic energy of the solitary wave overtopping flow for various seawall sections and wave scenarios. In addition to type 2 and 3 waves as presented in Section 3, six more solitary waves are considered (see Table 2). The water depths for the wave case group 1 (type 4, 5, 2 and 6) and group 2 (type 7, 3, 8 and 9) are 0.22 m and 0.256 m, respectively, and the wave heights in each group are presented in an ascending order. The seawall section is changed by varying its slope. As shown in Fig. 9, the coordinates $(x3, y3)$, $(x4, y4)$ and $(x5, y5)$ are fixed, and $(x2, y2)$ shifts along the red-dash line to get the slopes of S1 = 0.25 (the cases presented in Section 3), S2 = 0.5, S3 = 1, S4 = 2 and S5 = infinite (vertical sea wall). The hydrodynamic characteristics of the overtopping wave in the 40 cases are investigated.

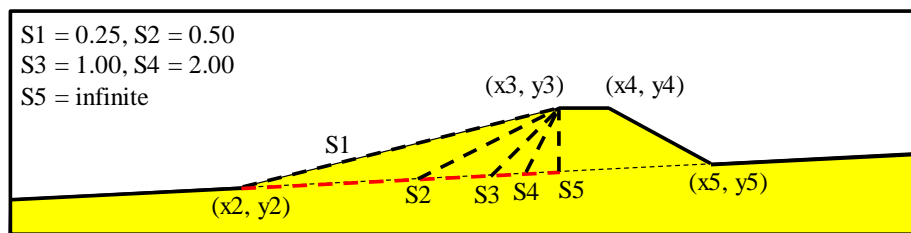Fig. 9. Schematic view of different seawall cross sections

Table 2. Wave parameters and wave overtopping volume in all cases

	Case number	h_0 (m)	H_0 (m)	Volume of solitary wave (m^3/m)	Wave overtopping volume (0.001 m^3/m)				
					S1	S2	S3	S4	S5
Group 1	T4	0.22	0.044	2.50	10.3	10.0	9.6	8.9	8.7
	T5		0.055	2.79	14.2	14.0	13.1	12.3	12.5
	T2		0.064	3.01	17.3	16.9	16.1	15.2	15.3
	T6		0.077	3.31	21.6	20.9	20.1	19.4	19.8
Group 2	T7	0.256	0.051	3.38	31.6	31.3	31.0	30.2	29.6
	T3		0.059	3.63	35.7	35.7	35.3	34.2	33.9
	T8		0.077	4.14	43.6	43.9	43.4	42.0	41.7
	T9		0.090	4.48	49.4	49.8	49.4	47.7	47.3

4.1. Influence of seawall section on the volume of overtopping wave

The wave overtopping volume (per unit length of the seawall) of each case is presented in Table 2 and Fig. 10. Generally, the wave overtopping increases with wave height and water level. Much more wave overtopping occurs if the still water level is higher. Specifically, of the same wave height, the water depth of T8 is about 16% higher than that of T6, but the wave overtopping in T8 is more than double of that in T6 for all the seawall sections. The practical implication is that as the sea level rises, the ocean waves possess much greater threats to the coastal structures.
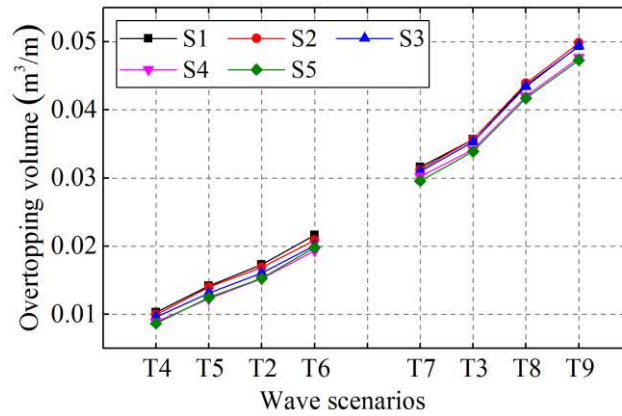

Fig. 10. Wave overtopping volumes in the studied cases

For each wave scenario, the overtopping volume in different seawall slopes (or sections) is normalized by the overtopping volume of S1, as shown in Fig. 11. Generally, a steeper seawall stops more seawater and hence reduces wave overtopping within a certain range, because it applies larger horizontal forces to the waves and more wave reflections occur. The wave overtopping for group 1 and group 2 solitary waves is reduced by around 12.5% and 5% respectively when the seawall slope increases from 0.25 (S1) to 2 (S4). It means that when the water depth (the local sea level raised by a real tsunami event) is higher, increasing the seawall slope becomes less effective in reducing wave overtopping. In this situation, a more effective way is to increase the height of the seawall, which however, is very costly. In group 2 waves, the overtopping volume of S5 is almost the same as that of

15

S4. In group 1 waves, the overtopping of S5 is even more than that of S4. It means that when the slope of the seawall reaches a certain value, further increasing the slope will not enhance the performance of a seawall in intercepting the overtopping wave, for the studied wave scenarios.
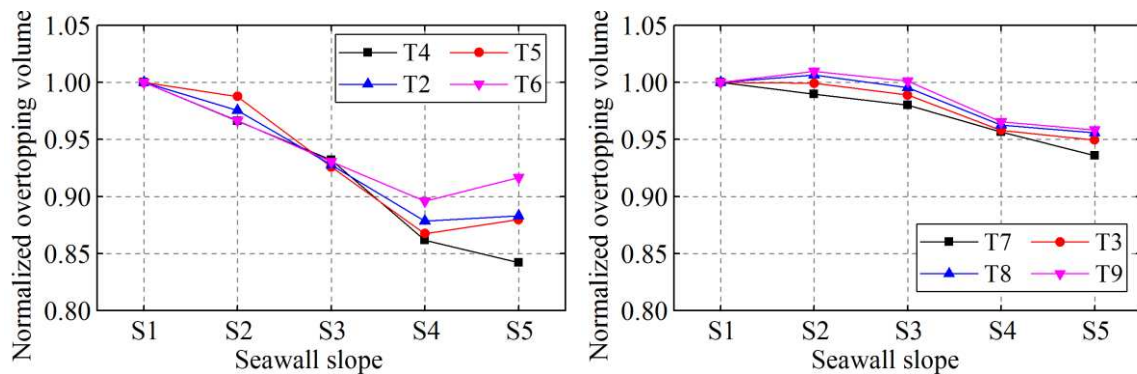

Fig. 11. Normalized wave overtopping volume against slope of seawall

Integrating the first-order solitary wave equation with respect to x gives the volume (per unit length) of the bulge part of a solitary wave (the light blue shade area in Fig. 1). This parameter is used as an indicator of the scale of the incident solitary wave. The ratio of the overtopping volume to the volume of the incident solitary wave is shown in Fig. 12. The volume percentages are about 25% and 50% for group 1 and group 2 solitary waves, respectively. In reality, the wave celerity and height of a tsunami can always be measured by a warning system. The above findings on the overtopping volume percentages provide a guidance in the estimation of tsunami overtopping magnitude. Fig. 12 also shows that increasing the slope of the seawall (from S1 to S4) helps to reduce the wave overtopping, although the effect for group 2 waves is marginal.
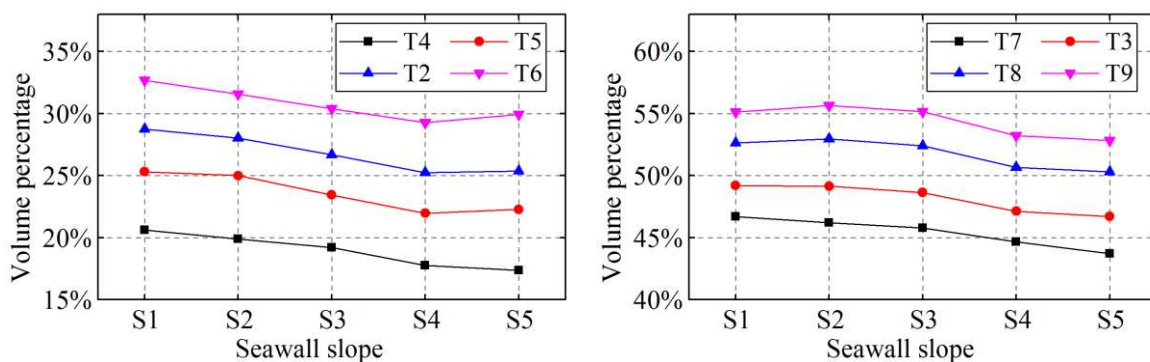

Fig. 12. Ratio of the overtopping volume to the volume of the bulge part of a solitary wave

4.2. Influence of seawall section on the kinetic energy of overtopping wave

The overtopping volume can be used as an indicator of the coastal flooding intensity, but it is also of great significance to investigate the destructive power that the overtopping waves carry, because lots of public facilities and buildings are built near the coastline. To quantify this effect, the kinetic energy (KE) of the overtopping wave computed as $\sum 0.5mv^2$ is presented in Fig. 13. It shows that the overtopping in Group 2 wave scenarios has much more KEs than the group 1 waves. The wave energy

has to be dissipated via the wave impact on coastal structures, erosion of the leeside of the seawall or the inland inundation, all of which should cause damages and/or disasters to the coastal areas. In contrast to the group 1 waves, whose overtopping KEs increase gently with the wave height, the KEs in group 2 waves increase considerably (around 2.5 times from T7 to T9). This is because the water depth (the local sea level raised by a real tsunami event) is quite high and hence the seawall is hard to stop the vast wave overtopping. This shows the high risk of coastal areas in the background of global sea level rising.
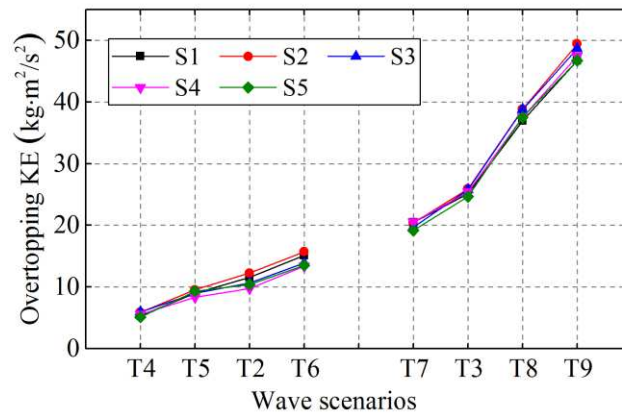

Fig. 13. KEs of the overtopping wave in the studied cases

The KE of the bulge part of a solitary wave can be approximated by assuming that all the fluid particles move with the wave celerity c, the ratio of the overtopping wave KE to which is shown in Fig. 14. The KE density of the overtopping wave evaluated by $\sum 0.5\rho v2$ is also evaluated (see Fig. 15). In all the wave scenarios, the seawall slope has little effect on the KE and KE density of the overtopping wave. For group 1 waves, around 12% of the solitary wave KE is transferred to the back of the seawall. This amount is more than double (~25%) for group 2 waves. The KE density for group 2 waves is about 30% larger than that for group 1 waves. Both the KE percentage of the overtopping wave and the KE density should provide useful guidance in estimating the destructive power of the tsunami overtopping in a real event. In addition, the results show that the wave overtopping in the circumstance of higher water depth is much more disruptive.
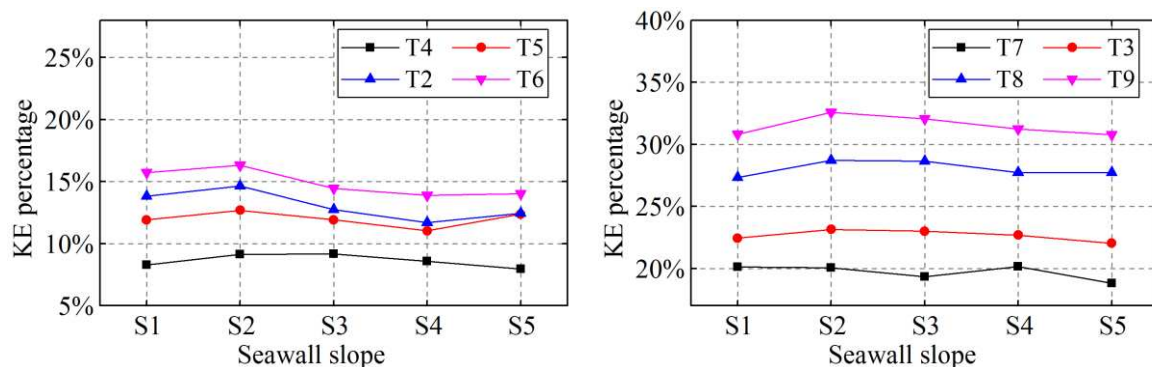

Fig. 14. Ratio of overtopping KE to the KE of the bulge part of a solitary wave
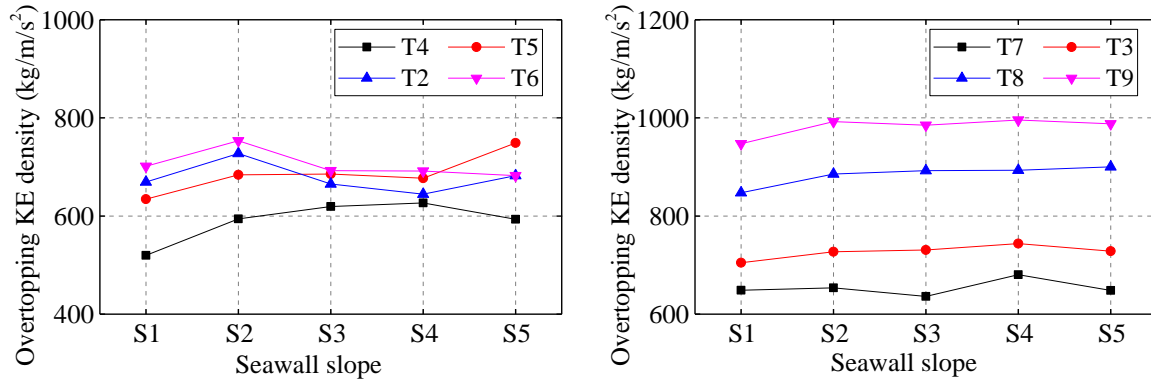
Fig. 15. Kinetic energy density of the overtopping wave

5. Conclusions

In this study, a mesh-free CPM based numerical wave flume is developed to study the solitary wave impinging and overtopping on an impermeable seawall. The CPM computes the gradient and Laplacian operators in the governing equations in a way consistent with the Taylor series expansion, achieving better numerical consistency and accuracy. By using the numerical wave flume, a documented experimental case is revisited. The wave fragmentation/coalescent and wave impact pressure/force predicted by CPM are in good agreement with the experimental data and benchmark numerical results.

Using the validated numerical wave flume, the characteristics of solitary wave overtopping are investigated thoroughly by varying the seawall section and the incident wave condition. It is found that in the tsunami event involving a higher water depth, the overtopping volume and the accompanied kinetic energy of the overtopping flow can be much more intensive. This implies that the seaside cities are exposed to higher risks of coastal inundation and facility/building damage in the background of global sea level rising. Increasing the slope of the seawall can reduce the tsunami overtopping in some extent, but it is not so effective especially when the water level is high. The percentages of the tsunami overtopping volume and kinetic energy compared with those of the bulge part of the incident wave are also evaluated. The data provides some helpful guidelines in the estimation/assessment of the intensity and hazardous effect of a real tsunami in practical field.

The CPM has intrinsic advantages in terms of the derivative computation. Comprehensive analyses of the energy and volume conservation of CPM are ongoing and will be presented in a future article.

6. Acknowledgement

References

[1] Wikipedia. 2006 Pangandaran earthquake and tsunami. 2006; Webpage: https://en.wikipedia.org/wiki/2006_Pangandaran_earthquake_and_tsunami.

[2] Oskin B. Japan Earthquake & Tsunami of 2011: Facts and Information. 2017; Webpage: https://www.livescience.com/39110-japan-2011-earthquake-tsunami-facts.html.

[3] Wikipedia. 2018 Sulawesi earthquake and tsunami. 2018; Webpage: https://en.wikipedia.org/wiki/2018_Sulawesi_earthquake_and_tsunami.

[4] Synolakis CE. The runup of solitary waves. Journal of Fluid Mechanics 2006;185:523-545.

[5] Briggs MJ, Synolakis CE, Harkins GS and Green DR. Laboratory experiments of tsunami runup on a circular island. Pure and applied geophysics 1995;144(3-4):569-593.

[6] Madsen PA, Fuhrman DR and Schäffer HA. On the solitary wave paradigm for tsunamis. Journal of Geophysical Research 2008;113(C12).

[7] Qu K, Ren XY and Kraatz S. Numerical investigation of tsunami-like wave hydrodynamic characteristics and its comparison with solitary wave. Applied Ocean Research 2017;63:36-48.

[8] Goring DG. Tsunamis-the propagation of long waves onto a shelf. 1978, PhD thesis, California Institute of Technology.

[9] Lin P and Liu PL-F. Internal wave-maker for Navier-Stokes equations models. Journal of waterway, port, coastal, and ocean engineering 1999;125(4):207-215.

[10] Ha T, Lin P and Cho Y-S. Generation of 3D regular and irregular waves using Navier–Stokes equations model with an internal wave maker. Coastal Engineering 2013;76:55-67.

[11] Liu X, Lin P and Shao S. ISPH wave simulation by using an internal wave maker. Coastal Engineering 2015;95:160-170.

[12] Lin P, Chang K-A and Liu PL-F. Runup and rundown of solitary waves on sloping beaches. Journal of waterway, port, coastal, and ocean engineering 1999;125(5):247-255.

[13] Lo EYM and Shao S. Simulation of near-shore solitary wave mechanics by an incompressible SPH method. Applied Ocean Research 2002;24(5):275-286.

[14] Hsiao S-C and Lin T-C. Tsunami-like solitary waves impinging and overtopping an impermeable seawall: Experiment and RANS modeling. Coastal Engineering 2010;57(1):1-18.

[15] Wu Y-T, Hsiao S-C, Huang Z-C and Hwang K-S. Propagation of solitary waves over a bottom-mounted barrier. Coastal Engineering 2012;62:31-47.

[16] Aristodemo F, Tripepi G, Meringolo DD and Veltri P. Solitary wave-induced forces on horizontal circular cylinders: Laboratory experiments and SPH simulations. Coastal Engineering 2017;129:17-35.

[17] Liang D, Jian W, Shao S, Chen R and Yang K. Incompressible SPH simulation of solitary wave interaction with movable seawalls. Journal of Fluids and Structures 2017;69:72-88.

[18] Monaghan JJ. Simulating free surface flows with SPH. Journal of Computational Physics 1994;110(2):399–406.

[19] Liu GR and Liu MB. Smoothed Particle Hydrodynamics: A meshfree particle method. 2003, Singapore: World Scientific.

[20] Koshizuka S, Nobe A and Oka Y. Numerical analysis of breaking waves using the moving particle semi-implicit method. International Journal for Numerical Methods in Fluids 1998;26(7):751-769.

[21] Mokos A, Rogers BD, Stansby PK and Domínguez JM. Multi-phase SPH modelling of violent hydrodynamics on GPUs. Computer Physics Communications 2015;196:304-316.

[22] Shao S and Lo EYM. Incompressible SPH method for simulating Newtonian and non-Newtonian flows with a free surface. Advances in Water Resources 2003;26(7):787-800.

[23] Khayyer A, Gotoh H and Shao S. Enhanced predictions of wave impact pressure by improved incompressible SPH methods. Applied Ocean Research 2009;31(2):111-131.

[24] Liu X, Lin P and Shao S. An ISPH simulation of coupled structure interaction with free surface flows. Journal of Fluids and Structures 2014;48:46-61.

[25] Huang C, Zhang DH, Si YL, Shi YX and Lin YG. Coupled finite particle method for simulations of wave and structure interaction. Coastal Engineering 2018;140:147-160.

[26] Huang C, Zhang DH, Shi YX, Si YL and Huang B. Coupled finite particle method with a modified particle shifting technology. International Journal for Numerical Methods in Engineering 2018;113(2):179-207.

[27] Fourtakas G and Rogers BD. Modelling multi-phase liquid-sediment scour and resuspension induced by rapid flows using Smoothed Particle Hydrodynamics (SPH) accelerated with a Graphics Processing Unit (GPU). Advances in Water Resources 2016;92:186-199.

[28] Khayyer A, Gotoh H, Shimizu Y, Gotoh K, Falahaty H and Shao S. Development of a projection-based SPH method for numerical wave flume with porous media of variable porosity. Coastal Engineering 2018;140:1-22.

[29] Gotoh H and Khayyer A. On the state-of-the-art of particle methods for coastal and ocean engineering. Coastal Engineering Journal 2018;60(1):79-103.

[30] Ye T, Pan D, Huang C and Liu M. Smoothed particle hydrodynamics (SPH) for complex fluid flows: Recent developments in methodology and applications. Physics of Fluids 2019;31(1):011301.

[31] Rostami Varnousfaaderani M and Ketabdari MJ. Numerical simulation of solitary wave breaking and impact on seawall using a modified turbulence SPH method with Riemann solvers. Journal of Marine Science and Technology 2014;20(2):344-356.

[32] Koh CG, Gao M and Luo C. A new particle method for simulation of incompressible free surface flow problems. International Journal for Numerical Methods in Engineering 2012;89(12):1582–1604.

[33] Khayyer A and Gotoh H. Enhancement of stability and accuracy of the moving particle semi-implicit method. Journal of Computational Physics 2011;230(8):3093-3118.

[34] Khayyer A, Gotoh H, Shimizu Y and Gotoh K. On enhancement of energy conservation properties of projection-based particle methods. European Journal of Mechanics - B/Fluids 2017;66:20-37.

[35] Marrone S, Antuono M, Colagrossi A, Colicchio G, Le Touzé D and Graziani G. δ-SPH model for simulating violent impact flows. Computer Methods in Applied Mechanics and Engineering 2011;200(13-16):1526-1542.

[36] Sun PN, Colagrossi A, Marrone S, Antuono M and Zhang AM. Multi-resolution Delta-plus-SPH with tensile instability control: Towards high Reynolds number flows. Computer Physics Communications 2018;224:63-80.

[37] Meringolo DD, Colagrossi A, Marrone S and Aristodemo F. On the filtering of acoustic components in weakly-compressible SPH simulations. Journal of Fluids and Structures 2017;70:1-23.

[38] Lind SJ, Xu R, Stansby PK and Rogers BD. Incompressible smoothed particle hydrodynamics for free-surface flows: A generalised diffusion-based algorithm for stability and validations for impulsive flows and propagating waves. Journal of Computational Physics 2012;231(4):1499-1523.

[39] Khayyer A, Gotoh H and Shimizu Y. Comparative study on accuracy and conservation properties of two particle regularization schemes and proposal of an optimized particle shifting scheme in ISPH context. Journal of Computational Physics 2017;332:236-256.

[40] Luo M, Koh CG and Bai W. A three-dimensional particle method for violent sloshing under regular and irregular excitations. Ocean Engineering 2016;120:52-63.

[41] Luo M, Koh CG, Gao M and Bai W. A particle method for two-phase flows with large density difference. International Journal for Numerical Methods in Engineering 2015;103(4):235-255.

[42] Chow AD, Rogers BD, Lind SJ and Stansby PK. Incompressible SPH (ISPH) with fast Poisson solver on a GPU. Computer Physics Communications 2018;226:81-103.

[43] Dilts GA. Moving least-squares particle hydrodynamics II: conservation and boundaries. International Journal for Numerical Methods in Engineering 2000;48(10):1503-1524.

[44] Luo M and Koh CG. Shared-Memory parallelization of consistent particle method for violent wave impact problems. Applied Ocean Research 2017;69:87-99.

[45] Ishikawa N, Beppu M, Mikami T, Tatesawa H and Asai M. Collapse mechanism of seawalls by impulsive load due to the March 11 tsunami. in 9th International Conference on Shock & Impact Loads on Structures. 2011. Fukuoka, Japan.

[46] Kudale MD and Kobayashi N. Hydraulic stability analysis of leeside slopes of overtopped breakwaters. Coastal Engineering 1996:1721-1734.